Chapter 3

A model for sand ridges in the shelf: effect of tidal and steady currents

In chapter 2 the dynamics of the small perturbations of a basic state consisting in a steady longshore current on a sloping bottom has been studied. Although the model predicted bedforms with the shape and the alongshore space of the shoreface–connected sand ridges, a model that includes the effect of the tidal currents is needed to explain the presence of these features in places as the Dutch coast, where significant tidal currents are present. In the present chapter a morphodynamic model will be discussed which explicitly describes the long-term interaction (i.e., averaged over many storm cycles) between a flow, consisting of both steady and tidal components, with the erodible bottom. Other new aspects are the incorporation of a cross-shore windstress and a statistical description of the sediment transport during storms and fair weather conditions, respectively.

There is a correlation, see Belderson (1986), between the type of dominant currents, stormy or tidaly, and the presence of differents large scale bed patterns. Previous studies have demonstrated that especially storm-driven currents are important for the evolution of shoreface-connected ridges (Swift *et al.*, 1978; Niedoroda *et al.*, 1984) and tidal currents are essential to generate tidal sandbanks (Zimmerman, 1981; Pattiaratchi & Collins, 1987). For tidal sandbanks idealized models have been developed and analyzed by Huthnance (1982), Hulscher *et al.* (1993) and de Swart & Hulscher (1995). The water motion is modelled by depth-averaged shallow water equations, the basic state describes a pure tidal current over a flat bottom and sediment transport is modelled as a local parametrization. The formation of sandbanks appears to be due to the combined effect of residual circulations, which develop due to tide-topography interactions, and a sediment flux which is a 'faster than linear' function of the current velocity (as occurs during fair weather conditions).

With regard to shoreface-connected sand ridges separate models have been studied, which are also based on the shallow water equations and a local sediment transport parametrization. Essential differences with the tidal sandbank models are that the basic state describes a steady current over a shelf with a transverse slope. The first model of this kind was presented by Trowbridge (1995) and a significant physical modifications of the model were added at chapter 2. There is explicitly modelled the momentum balance of the basic state flow and demonstrated the important role of a longshore pressure gradient for the ridge formation. Incorporation of the effect of local bedslopes on the sediment transport resulted in the prediction of preferred modes having the fastest growth rate. The spacings and migration speeds of these modes appeared to be in agreement with observations along the US and Dutch inner shelf. The main causes for the formation of shoreface-connected ridges are the transverse slope of the inner shelf, in combination with a sediment flux which is linear in the current (as occurs during stormy conditions). However, for the North Sea ridges the model is not entirely suitable since no tidal effects are incorporated.

As in previous studies it is shown that large-scale bedforms on the shelf can form as a free instability of a morphodynamic model which describes the interaction between depth-averaged

---

This chapter is part of the paper *A model for sand ridges on the shelf: effect of tidal and steady currents* submitted to the J. Geophys. Res., with co-authors H. E. de Swart and A. Falqués
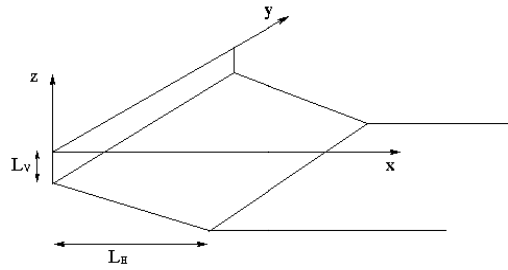
Figure 3.1: Sketch of the geometry and coordinate system. For explanation of the symbols see the text.

shallow water motion and the erodible bottom. The new aspects in this study are the explicit incorporation of both steady and tidal currents on a sloping bottom and a statistical approach to describe the sediment transport during storms (linear in the current) and fair weather conditions (cubic in the current). The present model is used to gain understanding of the different ridge characteristics in different geographical regions. This is done by analyzing the initial growth of small bottom perturbations, which evolve on a basic state describing a longshore uniform flow over a reference topography, with the use of spectral methods.

The first objective is to investigate the effect of tidal currents on the dynamics ofshoreface-connected sand ridges. Secondly, it will be demonstrated that the model also allows for different types of bedforms, including tidal sandbanks, and that the selection of the most preferred mode strongly depends on the storm fraction, the intensity of the tidal currents and the geometrical characteristics of the shelf. These results will also be explained in terms of different physical mechanisms. For high storm fractions only bedforms trapped to the inner shelf are generated. These bedforms, which resemble shoreface-connected sand ridges, have growth rates and migration speeds which decrease if the relative contribution of tides in the total current profile increases. Nevertheless, formation of bedforms still occurs even in case of a pure oscillatory current, due to the presence of the transversely sloping bottom. If also the effects of fair weather conditions are incorporated it is found that basically four other bottom modes can be generated: shoreface-connected sand ridges, Coriolis and frictionally-induced bars related to steady currents, trapped tidal ridges and tidal sandbanks. Their growth rates strongly depend on the weather climate and the geometrical characteristics of the shelf area. It will be demonstrated that these bedforms are related to different physical instability mechanisms.

The organization of the chapter is as follows. Equations of motion and boundary conditions are presented in section 3.1. This is followed by a discussion in section 3.2 of a reference state, which describes a longshore uniform flow with both steady and tidal components. The stability properties of this morphodynamic equilibrium with respect to small bottom perturbations are analyzed in section 3.3. Results are presented in the sections 3.4 and 3.5 and the final section contains the discussion and conclusions.

3.1   Governing equations and boundary conditions

Although the vertical structure of the currents can have an important role in the ridge area, it is hypothesized here that a depth-averaged model already can describe the ridge formation. So we will consider the 2D shallow water momentum equations

$$\frac{\partial \boldsymbol{v}}{\partial t} + (\boldsymbol{v} \cdot \boldsymbol{\nabla})\boldsymbol{v} + f\boldsymbol{e}_z \times \boldsymbol{v} = -g\boldsymbol{\nabla}z_s - \mu\frac{\boldsymbol{v}}{z_s - z_b} + \frac{\boldsymbol{\tau}^*}{\rho(z_s - z_b)}, \tag{3.1}$$

and the mass conservation equation:

$$\frac{\partial(z_s - z_b)}{\partial t} + \boldsymbol{\nabla} \cdot [(z_s - z_b)\boldsymbol{v}] = 0. \tag{3.2}$$

Here $\boldsymbol{v}$ is the depth-averaged velocity, f is the Coriolis parameter, $\boldsymbol{e}_z$ a unity vector in the vertical direction, z_s and z_b are the free surface and the bottom elevation, ρ is the water density, $\boldsymbol{\tau}^*$ is the

wind stress, g is the acceleration due to gravity and μ is a bottom friction coefficient. A linearized bed shear stress formulation is used in order to allow for a simple tidal current solution. This Lorentz linearization procedure is discussed in Zimmerman (1992).

The bottom evolution is considered to be governed by a sediment conservation equation:

$$\frac{\partial z_b}{\partial t} + \boldsymbol{\nabla} \cdot \boldsymbol{q} = 0, \tag{3.3}$$

where $\boldsymbol{q}$ stands for the volumetric sediment flux per unit width. A parametrization for this transport will be given later on.

The equations are considered on a half-open domain, as sketched in figure 3.1. An orthogonal coordinate system is taken, such that $x = 0$ marks the transition from inner shelf to shoreface, which is assumed to be parallel to the straight coastline. The x-, y- and z-axis thus point in the cross-shore, longshore and vertical direction, respectively. Here $z = 0$ represents the still water level and $\boldsymbol{\nabla} = (\partial/\partial x, \partial/\partial y)$. The boundary conditions imposed are that both the cross-shore flow component u and the bottom perturbation h vanish at $x = 0$ and far offshore (i.e., $x \to \infty$). This means that the presence of coastally trapped bedforms will be investigated and there is no net exchange between the inner shelf and the shoreface.

Note that the equations of motion discussed above are to be interpreted as describing the dynamics of the water motion and bed evolution averaged over many storm cycles (O(10 yr)). This means that the effect of fluctuations due to storms is only parametrically accounted for in the model. For a discussion about this aspect and about the justification of the boundary conditions see chapter 2 and appendix A.

Let us now make the equations of motion dimensionless. This is done by introducing the new dependent variables

$$t' = \sigma\, t, \qquad\qquad x' = x/L_s, \qquad\qquad y' = y/L_s,$$

where σ is the tidal frequency and L_s the characteristic width of the inner shelf. Furthermore we introduce the transformations

$$\boldsymbol{v} = U\boldsymbol{v}\,', \qquad z_b = L_v z_b', \qquad z_s = \frac{U\sigma L_s}{g} z_s', \qquad \boldsymbol{q} = [q]\,\boldsymbol{q}'$$

where U, L_v and $[q]$ are characteristic magnitudes for the current, the depth and the volumetric sediment flux per unit width. Here U and $[q]$ will be specified later on, whereas L_v will be the water depth at the transition $x = 0$ between the inner shelf and the shoreface.

If we drop the primes in the variables for convenience, the non-dimensional momentum and mass conservation equations read:

$$\frac{\partial \boldsymbol{v}}{\partial t} + \lambda(\boldsymbol{v} \cdot \boldsymbol{\nabla})\boldsymbol{v} + \hat{f}\boldsymbol{e}_z \times \boldsymbol{v} = -\boldsymbol{\nabla} z_s - \frac{r\,\boldsymbol{v}}{\hat{F}^2 z_s - z_b} + \frac{\boldsymbol{\tau}_s}{\hat{F}^2 z_s - z_b}, \tag{3.4}$$

$$\frac{\partial(\hat{F}^2 z_s - z_b)}{\partial t} + \lambda\boldsymbol{\nabla} \cdot ((\hat{F}^2 z_s - z_b)\boldsymbol{v}) = 0, \tag{3.5}$$

where $\lambda = U/(\sigma L_s)$, $\hat{f} = f/\sigma$, $r = \mu/(\sigma L_v)$, $\hat{F}^2 = F^2/\lambda$, $F = U/\sqrt{gL_v}$ and $\boldsymbol{\tau}_s = \boldsymbol{\tau}_s^*/(\rho\sigma U L_v)$. Typical values of the parameters are $\lambda \sim 1$, $\hat{f} \sim 0.8$, $r \sim 0.5$ and $|\boldsymbol{\tau}_s| \sim 0.1$. Since $U \sim 1$ ms^{-1} and $L_v \sim 20$ m the Froude number is very small ($F^2 \sim 0.005$). Therefore the free surface terms which are measured by $\hat{F}^2$ can be neglected in equations (3.4) and (3.5).

Now we turn to the sediment mass conservation equation (3.3). Using the previous scaling its dimensionless form reads (primes are again dropped)

$$\frac{\partial z_b}{\partial t} + \frac{[q]}{\sigma L_v L_s}\boldsymbol{\nabla} \cdot \boldsymbol{q} = 0.$$

Since $[q] \sim 10^{-5}$ m^{2}s^{-1} during storms, it follows that the parameter which measures the magnitude of the sediment flux divergence is very small. Thus the bottom does not evolve on the tidal timescale σ^{-1}, but rather on the morphological time scale $T_m = L_v L_s/[q]$, which is much longer: $T_m \sim 600$ yr. Consequently, the time derivative of the bedlevel z_b in equation (3.5) can be

neglected. Furthermore, the bottom evolution is not determined by the oscillatory sediment fluxes during the tidal cycle, but rather by the tidally averaged fluxes. Hence the final dimensionless bottom evolution equation becomes

$$\frac{\partial z_b}{\partial \tau} + \boldsymbol{\nabla} \cdot \langle \boldsymbol{q} \rangle = 0, \tag{3.6}$$

where $< . >$ denotes an average over the tidal period and $\tau = t/T_m$ is a slow nondimensional time coordinate.

Finally we discuss how the sediment transport is expressed in terms of the state variables of the system. In contrast to previous studies on this topic we distinguish between the transport during storm and that during fair weather situations. In appendix D it is explained that a simple parametrization which accounts for this effect is

$$\boldsymbol{q} = \beta \boldsymbol{q}_1 + (1 - \beta) \boldsymbol{q}_3 \qquad\qquad \boldsymbol{q}_m = \nu_m |\boldsymbol{v}|^m \left(\frac{\boldsymbol{v}}{|\boldsymbol{v}|} - \gamma \boldsymbol{\nabla} h \right). \tag{3.7}$$

Here β is the fraction of time during which storms occur with the sediment transport being linear in the depth-averaged velocity $\boldsymbol{v}$. During the other periods (fair weather conditions) the transport is cubic in the velocity. Here $\nu_3 = 1$ and $\nu_1 \gg 1$ is the squared ratio of the characteristic wave-related velocity amplitude and the velocity scale U. Note that the contribution of the linear sediment transport (i.e., during storms) to the total transport need not to be dominant, because in nature fair weather occurs more often than storms (in other words, fraction β is small).

The term involving the coefficient γ accounts for the preferred down-slope movement of sediment due to gravitational effects; typically $\gamma \sim 1$ and with the new scaling $\hat{\gamma} \sim 10^{-4}$. Note that the critical shear stress for erosion is not explicitly taken into account: it is assumed to be much smaller than the instantaneous shear stresses.

3.2 Basic state

We are now going to look for a basic state with a longshore current $\boldsymbol{v} = (0, V(x, t))$ over a sloping bottom $z_b = -H(x)$. In this state the current is allowed to vary with time but the net sediment transport must vanish so that the bottom does not vary on the morphological timescale. In this case the sediment and the mass conservation equations are automatically fulfilled so that we only have to consider the momentum equations (3.4) which become

$$-\hat{f}V = -\frac{\partial \xi}{\partial x} + \frac{\tau_{sx}}{H}, \qquad\qquad \frac{\partial V}{\partial t} = -\frac{\partial \xi}{\partial y} - r\frac{V}{H} + \frac{\tau_{sy}}{H}. \tag{3.8}$$

where $z_s = \xi(x, y, t)$ is the free surface elevation.

Note that in this model the longshore pressure gradient $\partial \xi / \partial y$ must be prescribed. The condition that the velocity profile must be longshore uniform and the solvability condition for the free surface imply that this forcing term can only be a function of time. Here we choose

$$\frac{\partial \xi}{\partial y} = s_0 - |s_1| \cos(t),$$

which represents a steady and one tidal component. From this the longshore flow $V(x, t)$ can be computed from the second equation in (3.8) whereas the first equation in (3.8) determines the cross-shore set-up or set-down of the water level due to cross-shore winds and Ekman effects. It is assumed that the windstress is constant and that the longshore windstress and longshore pressure gradient drive a current in the same direction. This implies that the parameters τ_{sy} and s_0 have opposite signs.

Upon writing the basic state velocity as a superposition of a steady and a time-dependent current, i.e. $V(x, t) = V_0(x) + V_1(x, t)$, the solution reads

$$V(x, t) = \alpha U_0(x) + (1 - |\alpha|) U_1(x) \sin(t + \varphi(x)) \tag{3.9}$$

with

$$\alpha = \frac{-s_0 + \tau_{sy}}{r}, \qquad\qquad U_0(x) = 1 + a[H(x) - 1], \qquad\qquad a = \frac{|s_0|}{|-s_0 + \tau_{sy}|},$$

$$U_1(x) = \frac{H}{\sqrt{H^2 + r^2}}, \qquad\qquad \varphi(x) = \arctan\left(\frac{r}{H}\right).$$

Here we have assumed that

$$|\alpha| + |s_1| = 1, \tag{3.10}$$

which states that the velocity scale U is defined as the maximum flow amplitude at the shoreface boundary $x = 0$. This quantity can be computed for a given longshore pressure gradient, longshore windstress, tidal frequency and water depth L_v at $x = 0$, because the applied scaling yields that

$$s_n = \frac{gs_n^*}{\sigma U} \qquad (n = 0, 1), \qquad\qquad \tau_{sy} = \frac{\tau_{sy}^*/\rho}{\sigma U L_v},$$

where the asterixes refer to dimensional variables.

The coefficient α is the dimensionless amplitude of the steady current at the transition $x = 0$ from the inner shelf to the shoreface. It also determines the relative contribution of the steady current to the *total* flow, i.e., $-1 \leq \alpha \leq 1$. In general the value of this parameter during storms will differ from that during mild weather. The steady flow is driven both by wind and a longshore pressure gradient; the relative effect of the latter to the total *steady* flow is measured by parameter a ($0 \leq a \leq 1$).

Finally, note that in case $|\alpha| = 1$ the reference state of the model becomes fully equivalent to that of chapter 2 with a linear bottom friction coefficient. Note that if in the present model a quadratic (rather than a linearized) bottom friction law would be used the tidal current profile would contain higher (odd) harmonics. As their incorporation would significantly complicate the subsequent analysis (cf. Zimmerman, 1992) without adding new physical insight, they are not considered here.

3.3   Linear stability analysis

The next step is to investigate the possible formation of bedforms, with a rhythmic structure in the alongshore direction, as free modes which evolve on the basic state of the previous section. This implies a study of the stability properties of the basic state with respect to small bottom perturbations. The procedure will be to solve the three hydrodynamic equations (3.4) and (3.5) on the tidal timescale to find the velocity and the free surface elevation as a function of a fixed given bottom topography. Next, we will substitute the flow variables in the bottom evolution equation (3.6) and we will solve it on the morphological timescale.

Thus we consider solutions of the form

$$\boldsymbol{v} = (u', V + v'), \qquad\qquad z_s = \xi + \eta', \qquad\qquad z_b = -H + h'.$$

Here the perturbations u', v' and η' in the water motion are functions of x, y, t and τ, whereas the bottom perturbation h' only depends on x, y and τ. After substitution in the equations of motion we use the properties of the known basic state to arrive at equations for the perturbations. Since we assume the latter to have small amplitudes, the resulting equations are linearized. Due to their structure and the imposed boundary conditions, they describe solutions with a periodic structure in the longshore direction, e.g. $u'(x, y, t) = \text{Re}\,[\tilde{u}(x, t, \tau)\exp(iky)]$, where k is the wavenumber.

The linearized equations for the amplitudes of the perturbations read

$$\frac{\partial \tilde{u}}{\partial t} + ik\lambda V\tilde{u} - \hat{f}\tilde{v} = -\frac{\partial \tilde{\eta}}{\partial x} - \frac{r}{H}\tilde{u} + \frac{\tau_{sx}}{H^2}\tilde{h} \tag{3.11a}$$

$$\frac{\partial \tilde{v}}{\partial t} + \lambda\left[\frac{\partial V}{\partial x}\tilde{u} + ikV\tilde{v}\right] + \hat{f}\tilde{u} = -ik\tilde{\eta} - \frac{r}{H}\tilde{v} + \frac{s_0}{H}\tilde{h} - rV_1\frac{\tilde{h}}{H^2} \tag{3.11b}$$

$$H\frac{\partial \tilde{u}}{\partial x} + \frac{dH}{dx}\tilde{u} + ikH\tilde{v} - ikV\tilde{h} = 0 \tag{3.11c}$$

$$\frac{\partial \tilde{h}}{\partial \tau} + \beta\langle\tilde{S}_1\rangle + (1 - \beta)\langle\tilde{S}_3\rangle = 0 \tag{3.11d}$$

Here

$$\tilde{S}_m = \nu_m |V|^{m-1} \left\{ \frac{(m-1)}{V} \frac{\partial V}{\partial x} \tilde{u} + \frac{\partial \tilde{u}}{\partial x} + ikm\tilde{v} \right.$$
$$\left. - \hat{\gamma}|V| \left(\left(\frac{m}{V} \frac{\partial V}{\partial x} \frac{\partial \tilde{h}}{\partial x} + \frac{\partial^2 \tilde{h}}{\partial x^2} \right) - k^2 \tilde{h} \right) \right\}$$

denotes the amplitude of the perturbed sediment flux divergence during storms ($m = 1$) and fair weather ($m = 3$), respectively. Note that the hydrodynamical problem for a specific reference bottom $H(x)$, as defined by equations (3.11a)-(3.11c), is solved separately for the two different flow regimes occurring in the model. The latter correspond to storms ($\beta = 1$) and fair weather conditions ($\beta = 0$), respectively. Ultimately, these results are combined in a statistical sense in the bottom evolution equation (3.11d) to solve for the bottom perturbations.

The amplitude equations have solutions of the type

$$(\tilde{u}(t,\tau), \tilde{v}(t,\tau), \tilde{\eta}(t,\tau), \tilde{h}(\tau)) = \mathrm{e}^{\omega \tau} (u(t), v(t), \eta(t), h) \tag{3.12}$$

where ω is a complex frequency which describes the evolution of the amplitudes on the morphological timescale and is to be determined from the dynamics. Its real part, $\Omega_r = \mathrm{Re}[\omega]$ is the growth rate of the perturbations and $c = -\mathrm{Im}[\omega]/\mathrm{k}$ is the corresponding phase speed.

First we analyze the dynamics on the short, tidal timescale. From cross-differentiation of the momentum equations (3.11a) and (3.11b) and substituting (3.12), we obtain the Fourier-transformed vorticity equation:

$$\left(\frac{\partial}{\partial t} + ik\lambda V \right) \left(\frac{\partial v}{\partial x} - iku \right) + \lambda u \frac{\partial^2 V}{\partial x^2} + \left(\hat{f} + \lambda \frac{\partial V}{\partial x} \right) \left(ikv + \frac{\partial u}{\partial x} \right) =$$
$$-\frac{r}{H} \left(\frac{\partial v}{\partial x} - iku \right) + \frac{r}{H^2} \frac{dH}{dx} v + s_0 \frac{\partial(h/H)}{\partial x} - r \frac{\partial}{\partial x} \left(V_1 \frac{h}{H^2} \right) - ik \frac{\tau_{sx}}{H^2} h. \tag{3.13}$$

Here the first term on the left-hand side describes the change of relative vorticity in a frame moving with the basic state velocity, the second term is the advection of basic vorticity by the perturbed flow and the third contribution describes vortex stretching. On the right-hand side we have the dissipation of vorticity and next three bottom frictional torques: one related to the perturbed flow moving along the reference bottom and two related to the steady and tidal flow moving along the perturbed bottom. The last term on the right-hand side is the torque induced by the cross-shore windstress.

From the continuity equation (3.11c) and (3.12) it follows the alongshore velocity perturbation as a function of h and u:

$$v = \frac{V}{H} h + \frac{i}{k} \left(\frac{\partial u}{\partial x} + \frac{1}{H} \frac{dH}{dx} u \right), \tag{3.14}$$

Substitution of this expression in (3.13) yields a single equation for the cross-shore velocity, u, as a function of the bottom perturbation, h:

$$\mathcal{U}_{12} \frac{\partial^3 u}{\partial t \partial x^2} + \mathcal{U}_{11} \frac{\partial^2 u}{\partial t \partial x} + \mathcal{U}_{10} \frac{\partial u}{\partial t} + \mathcal{U}_{02} \frac{\partial^2 u}{\partial x^2} + \mathcal{U}_{01} \frac{\partial u}{\partial x} + \mathcal{U}_{00} u = \mathcal{H}_1 \frac{\partial h}{\partial x} + \mathcal{H}_0 h \tag{3.15}$$

where the coefficients are specified in appendix E. Note that this so-called 'flow over topography' problem is governed by a vorticity equation, as in Hulscher *et al.* (1993) and de Swart & Hulscher (1995), although equation (3.15) is formulated in terms of the cross-shore velocity perturbation.

The linearized bottom evolution equation (3.6) becomes, after substitution of (3.12) and (3.14):

$$\omega h = -\beta \langle S_1 \rangle - (1-\beta) \langle S_3 \rangle \tag{3.16}$$

where

$$S_m = -\nu_m |V|^{m-1} \left\{ (m-1) \frac{\partial u}{\partial x} + \left(\frac{m}{H} \frac{dH}{dx} - \frac{(m-1)}{V} \frac{dV}{dx} \right) u \right.$$
$$\left. -ikm \frac{V}{H} h + |V| \left(\hat{\gamma} \left(\frac{\partial^2 h}{\partial x^2} + \left(\frac{m}{V} \frac{dV}{dx} \right) \frac{\partial h}{\partial x} \right) - \hat{\gamma} k^2 h \right) \right\} \tag{3.17}$$

Together with the boundary conditions $u(0) = u(\infty) = 0, h(0) = h(\infty) = 0$, equations (3.15)-(3.17) define an eigenvalue problem which determines the complex frequency ω of the perturbations as a function of the wavenumber k and the model parameters. This problem is solved by a numerical spectral method (collocation in x, Fourier-Galerkin in t, see appendix E for details).

The physical interpretation of the different terms in (3.17) is as follows. The terms multiplied by the coefficient $\hat{\gamma}$ describe a diffusive decay of the bedforms. The term in equation (3.17) preceding the diffusive contributions is proportional to ih and therefore describes a migration of bedforms. The remaining contributions are potential sources of instabilities and they appear to be of three different kinds. The first term is due to spatial gradients in the cross-shore flow perturbations and requires a sediment transport which is 'faster than linear' in the flow velocity, i.e., $m > 1$. In case of steady flows this is the source of instability which often appears in river models, see Schielen *et al.* (1993) and references herein. The mechanism also appears in the tidal morphological models of Huthnance (1982) and de Swart & Hulscher (1995). The second term is active if the reference topography contains a cross-shore gradient. In the case that $m = 1$, which is considered by Trowbridge (1995), this is the only source of morphologic instabilities, see also chapter 2. Finally, the third term only contributes to the bottom evolution if the basic flow contains cross-shore shear ($\partial V/\partial x \neq 0$) and for $m > 1$. Its effect for steady longshore flow is considered in Falqués *et al.* (1996).

3.4 Results

3.4.1 Introductory remarks

We now discuss the results which are obtained with a numerical model which solves the morphological stability of the basic state, consisting of both tidal and steady currents over a given reference topography. This numerical model is called MORFO30, to distinguish it from the MORFO20-model for pure steady currents which is discussed in chapter 2.

The required input of the model consists of the shelf and flow characteristics of the reference state. It is important to realize that many of the model parameters (in particular those related to the forcing and dissipation mechanisms) generally have different values during storms than during fair weather conditions. These values will be frequently varied and discussed in the experiments to be reported in the next subsections. Here we will only specify default values of the part of the input which is independent of the flow regime, i.e., the tidal frequency σ, the Coriolis parameter f and the shelf characteristics. They are chosen such that they are representative for the situation on the shelf along the Central Dutch coast. Here the tidal frequency is $\sigma = 1.4 \times 10^{-4}$ s^{-1} and $f = 1.12 \times 10^{-4}$ s^{-1}, consequently the nondimensional parameter $\hat{f} = 0.8$. Furthermore, the inner shelf has a width $L_s = 12 \times 10^3$ m and a rather constant slope, the water depth at the transition inner shelf-shoreface is $L_v = 15$ m and the outer shelf has a constant depth of 20 m. This motivates the choice of the following dimensionless reference topography:

$$H(x) = \begin{cases} 1 + sx & \text{if } 0 \leq x < 1, \\ 1 + s & \text{if } x \geq 1. \end{cases} \tag{3.18}$$

where $s = s_* L_s / L_v$ and s_* the shelf slope; here s=0.33 is considered.

3.4.2 Storm-dominated shelves: $\beta = 1$

Here we consider the new model in case that the shelf is storm-dominated, i.e., $\beta = 1$. The morphological timescale is chosen such that parameter $\nu_1 = 1$ in equation (3.17). This implies that $T_m \sim 600$ yr. Other default parameter values in these experiments are: a dimensional friction parameter $\mu = 1.25 \times 10^{-3}$ ms^{-1} and a bed slope coefficient $\gamma = 0.1$. This yields for the nondimensional parameters $r = 0.2$, and $\hat{\gamma} = 10^{-4}$. The cross-shore windstress τ_{sx}, the velocity amplitude U and the tidal current parameter α will be varied. Test runs showed that in this case accurate results are obtained with $N = 60$ collocation points and $M = 3$ Fourier modes in time (representing the principal tidal component and two overtides).

In the first experiment tidal currents are neglected, i.e., $\alpha = \pm 1$. The velocity amplitude is taken to be $U = 0.25$ ms^{-1}, which implies that parameter $\lambda^{-1} = 6.8$. The new element here with

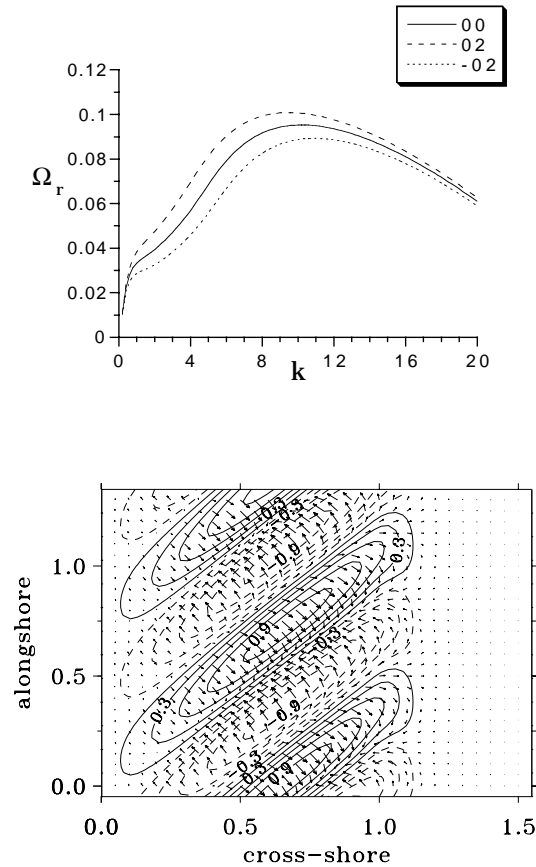Figure 3.2: Growth rate Ω_r versus wavenumber k for different values of the cross-shore windstress on a storm-dominated shelf. Solid line: $\tau_{sx} = 0$, dashed curve: $\tau_{sx} = 0.2$, dotted curve: $\tau_{sx} = -0.2$. For other parameter values see the text. In b. contour levels of the most preferred bottom mode are shown, together with the perturbed velocity field; note the offshore deflection of the current over the bars.
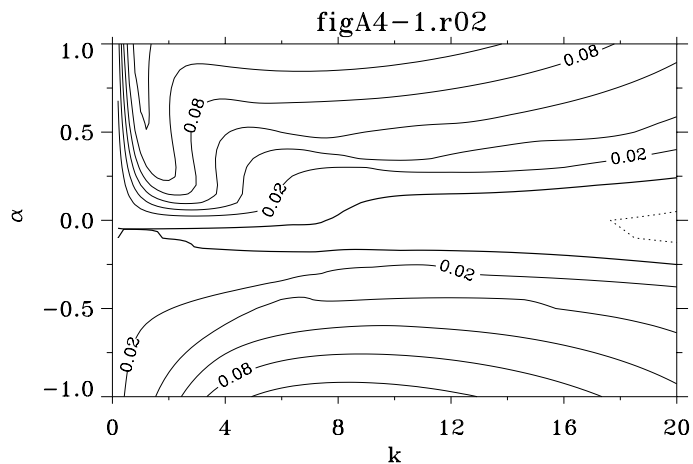

Figure 3.3: Contour plot of the largest growth rate of perturbations as a function of wavenumber k and parameter α, which defines the relative contribution of the steady flow to the total flow. Storm-dominated case, for parameter values see the text.

respect to chapter 2 is that different values of the cross-shore windstress τ_{sx} are considered. Apart from that these results serve as a test to check the validity of the MORFO30-model.

In figure 3.2a the growth rate versus the wavenumber is shown for $\alpha = -1$ and $a = 1$, a
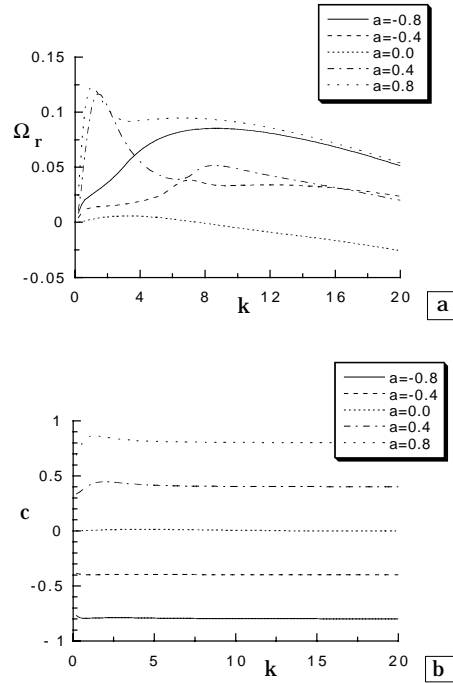
Figure 3.4: a. Growth rate Ω_r versus wavenumber k for different values of parameter α; storm-dominated case. Other parameters as in the previous plot. b. As a., but for the migration speed c.
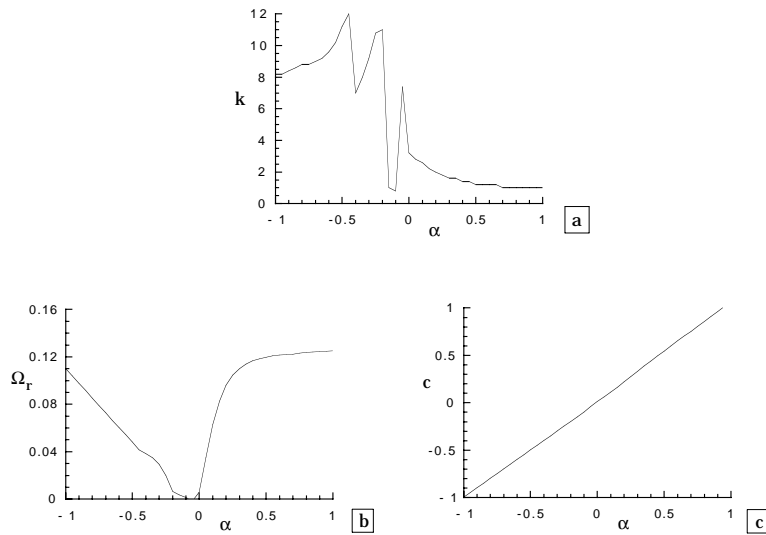

Figure 3.5: a. Wavenumber for which the maximum growth rate is attained as a function of parameter α; other parameter values as in figure 3.3. b. As a., but for the maximum growth rates. c. As a., but the migration speed of the most preferred bedforms.

parameter set which is also investigated in chapter 2. This describes a reference flow which points in the negative y-direction and is forced by a longshore pressure gradient. The curves of the growth rates all attain a maximum for wavenumber $k = \mathcal{O}(10)$. Since this quantity is made dimensionless with the shelfwidth L_s, this implies that the preferred modes have a longshore wave-length of approximately 7-8 km.

The spatial structure of the bars with the largest growth rate, together with the perturbed velocity field, is shown in figure 3.2b for $\tau_{sx} = 0.2$. Clearly the bars are rotated upcurrent and
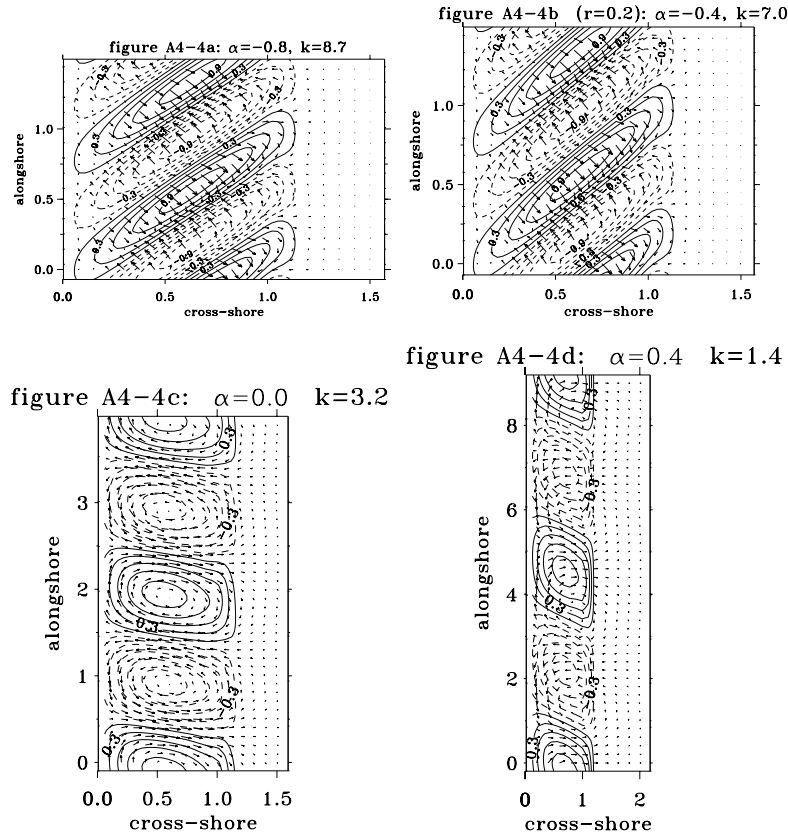
Figure 3.6: Spatial patterns of the most preferred bedforms for different values of parameter α, other parameter values as in figure 3.3. a. $\alpha = -0.8, k = 8.7$. b. $\alpha = -0.4, k = 7.0$. c. $\alpha = 0., k = 3.2$. d. $\alpha = 0.4, k = 1.4$.
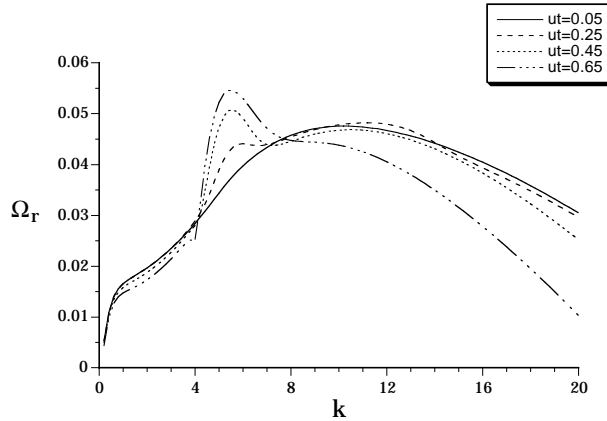

Figure 3.7: Growth rate versus the wavenumber for a fixed steady current (velocity $U_s = 0.25 \text{ ms}^{-1}$ towards the south) and different tidal current amplitudes U_t. Growth rates have been made nondimensional with the morphological timescale for $U = U_s + U_t = 0.5 \text{ ms}^{-1}$. The friction parameter is $r = 0.2$ and other parameter values are as in the previous experiments.

there is an offshore deflection of the flow over the crests. Both the structure and the wave-length of these bars correspond well with those of observed shoreface-connected sand ridges in the field. Since the morphological timescale $T_m \sim 600$ years a dimensionless growth rate of 0.1 corresponds to a dimensional e-folding timescale of 6000 years. Furthermore, the dimensionless migration speeds (not shown) are $c \sim -1$. This means that the ridges move downstream with a velocity of about 20 m yr^{-1}. Also these values are in reasonable agreement with the observations.

Note that offshore windstresses enhance the growth rates of the bedforms. This can be understood from the physical arguments discussed in chapter 2. The instability process is controlled by the so-called transverse slope mechanism which requires offshore (inshore) deflection of the currents over the bars (troughs) and this occurs if the crest-lines are rotated upcurrent. Now in the case of an offshore directed windstress the water parcels experience an additional offshore deflection above the bars due to the force $\tau_{sx} h / H^2$ which appears in the cross-shore momentum balance (3.11a), hence the growth rates become larger. As can be seen the preferred wavenumber, which has the largest growth rate, shifts to smaller values if τ_{sx} becomes larger.

In the next set of experiments the parameter $\tau_{sx} = 0$, the velocity scale is taken to be $U = 0.5\ \mathrm{ms}^{-1}$ (hence $\lambda^{-1} = 3.4$) and the parameter α is varied. According to equations (3.9)-(3.10) this implies that the intensity of both the steady and tidal current is varied, but the maximum velocity at $x = 0$ is kept fixed. In figure 3.3 a contour plot is shown of the growth rates of the bedforms in the $k - \alpha$ parameter space. In figure 3.4 the growth rates and migration speeds are shown versus the wavenumber for different, but fixed values of α : $-0.8, -0.4, 0, 0.4$ and 0.8. We recall that e.g. $\alpha = 0.8$ means that the steady component in the total basic state flow near the landward boundary is 80 % and that a positive (negative) value for α in this case corresponds to a net flow in the positive (negative) y-direction. Each curve has a clear maximum which corresponds to the preferred wavenumber for this set of parameter values. In figure 3.5 the dominant wavenumber and corresponding growth rates and migration speeds are shown as functions of the parameter α. The discontinuities observed in the plots indicate transitions to another modenumber having the largest growth rate. Finally in figure 3.6 the spatial patterns of a few characteristic preferred bedforms and the perturbed tidally-averaged velocity field are shown for different values of α. Other experiments (not shown) have demonstrated that the results shown are quite generic for the model: they are only weakly sensitive to variations in the parameters r, f and λ.

Clearly these results show that growth rates and migration speeds decrease with decreasing values of $|\alpha|$. This means that with an increasing relative contribution of tides to the total velocity field, keeping the velocity scale U fixed, the instability process becomes less effective. However, a different conclusion is reached in case the steady velocity amplitude $U_s (\equiv (1 - |\alpha|)\, U)$ is kept fixed and next the tidal velocity amplitude $U_t (\equiv |\alpha| U)$ is increased. As shown in figure 3.7 increasing the tidal influence in an *absolute* sense results in *larger* growth rates. This is due to the fact that the total velocity scale U now increases, which causes the morphological timescale to become shorter (for storm conditions T_m is inversely proportional to U). Also here a transition between modenumbers is observed: one has a maximum amplification rate near $k \sim 10$) and the other attain a maximum growth rate near $k \sim 5$.

It is also remarkable that, for a fixed value of $|\alpha|$, the results strongly depend on the direction of the steady flow. This appears to be a consequence of earth rotation effects. In this sense it is useful to distinguish between upwelling and downwelling flow. The first (second) case refers to a situation during which the Ekman transport induced by Coriolis forces is directed offshore (onshore), which results in a set-down (set-up) of the sealevel and associated upwelling (downwelling). In the present model this occurs on the Northern Hemisphere for flow in the positive (negative) y-direction. Now the growth rates for downwelling flow appear to be much smaller than those for upwelling flow, the corresponding wave-lengths of the most preferred bottom modes are smaller and the bars have a different orientation. This will be further discussed in section 3.5. The overall characteristics are that all ridges are trapped to the inner shelf and that their crestlines are rotated upcurrent with respect to the steady current. It is important to realize at this point that all shoreface-connected ridges in the field occur for negative α (i.e., downwelling flow).

The third important result is that in case $\alpha = 0$ (tides only) there is positive feedback between the tidal current and the erodible bottom. According to figure 3.3 these growing modes seem to be connected to those which appear for positive α. This result clearly differs from the conclusions stated by Huthnance (1982) and Hulscher *et al.* (1993) that a 'faster than linear' sediment transport is required in order to generate bedforms due to tide-topography interaction. However, they considered a reference flow over a flat bottom, whereas in the present model the inner shelf has a transverse slope. In the next section it will be demonstrated, by using physical arguments, that indeed the presence of the transverse slope is responsible for the instability process in this case. From figure 3.6c it can be seen that the preferred bottom mode in case of pure tides has a longshore wave-length of about 20 km, which is close to the tidal excursion length $U_t T$ (U_t the tidal current amplitude, T the tidal period). Furthermore, the bar crests are rotated cyclonically with respect to
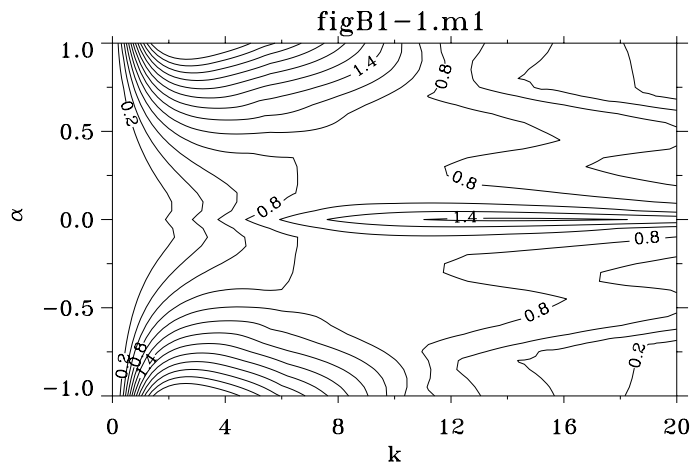
Figure 3.8: Contour plot of the maximum growth rate of perturbations as a function of wavenumber k and parameter α, which defines the relative contribution of the steady flow to the total flow. Fair weather conditions, for parameter values see the text.

the tidal current direction and anticyclonic residual circulations occur around the bars. However, the centre of these circulations are slightly shifted in the negative y-direction, with respect to the bar crests, such that there is again an offshore deflection of the net current over the bars. In case that $\alpha = 0$ a detailed analysis of the flow behaviour at different stages of the tidal cycle was carried out. From this it was found that, apart from residual circulations, the tide-topography interactions also generate M_4- and M_6-overtides with significant amplitudes. Thus the current near a ridge has a complicated temporal structure.

It is also worthwhile to point out that for $\alpha = 0$ and also $f = 0, r = 0$ the growth rates become infinitely large. This suggests that the instability mechanism cannot longer be described by a model which is based on irrotational flow, as was done by Trowbridge (1995) for steady flow. The reason for this is that tidally induced residual circulations around sandbanks can only exist if friction is present, see e.g. Zimmerman (1981). However it is still true that the transverse bed slope is the principal cause of instabilities on storm-driven shelves: if the slope $s \to 0$ growth rates tend to zero.

Finally note that the results are rather sensitive to parameter a in the steady flow, which indicates the relative contribution of longshore pressure gradients in driving the reference flow. If also the forcing due to a longshore windstress is taken into account growth rates become substantially smaller. This result was also found in chapter 2. There ussing statistical arguments, see appendix A, to argue that during stormy conditions the relative contribution of the longshore windstress is rather weak, because the effect is counteracted by a frictional stress related to the weather fluctuations. We will not pursue on this aspect here, but simply state that quite realistic ridges are obtained in case forcing by a longshore pressure gradient is used.

3.4.3   Fair weather conditions: $\beta = 0$

In this subsection the sediment transport is assumed to be cubic in the instantaneous flow velocity. This corresponds to fair weather conditions during which the wave orbital velocities near the bottom are small compared to the velocities induced by steady and tidal currents. In this case the morphological timescale T_m is defined such that parameter $\nu_3 = 1$ in equation (3.17). This means that the morphological timescale T_m is much larger than in the previous subsection: it is of order 6000 yr (since the ratio $(\nu_1/\nu_3) \sim 10$). Experiments revealed that in this case more collocation points were required to obtain converging solutions. The results described below have been computed for $N = 120$ collocation points and $M = 3$ tidal harmonics. Also the model yields spurious eigenvalues for certain combinations of the model parameters. Although partially visible in the results, this behaviour was not such that it masked the general behaviour of the model.

Here we present results for the same shelf as was discussed in the previous subsection. The following parameter values were used: $a = 1, f = 0.8, r = 0.4, \lambda^{-1} = 3.4$ and $\hat{\gamma} = 10^{-3}$. Further-
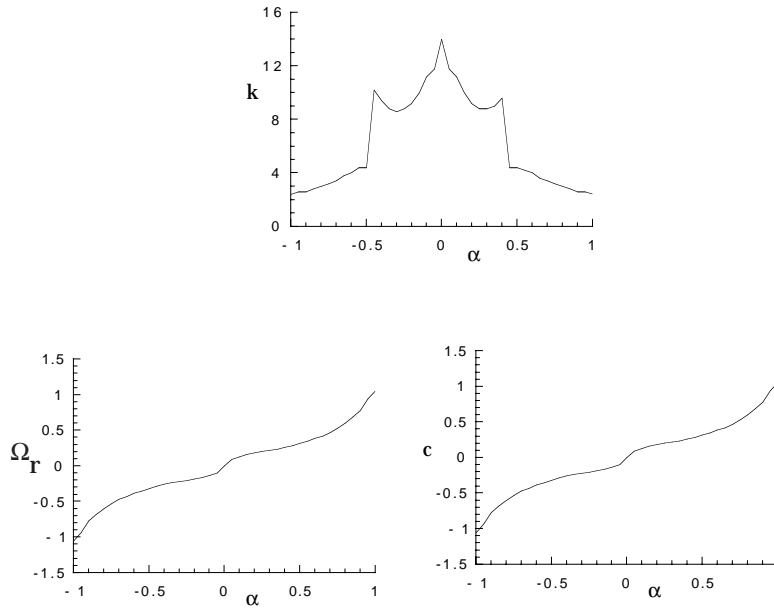
Figure 3.9: Wavenumber for which the maximum growth rate (top), the maximum growth rates (bottom left) and the migration speed of the most preferred bedforms (bottom right) is attained as a function of parameter α; other parameter values as in figure 3.8.
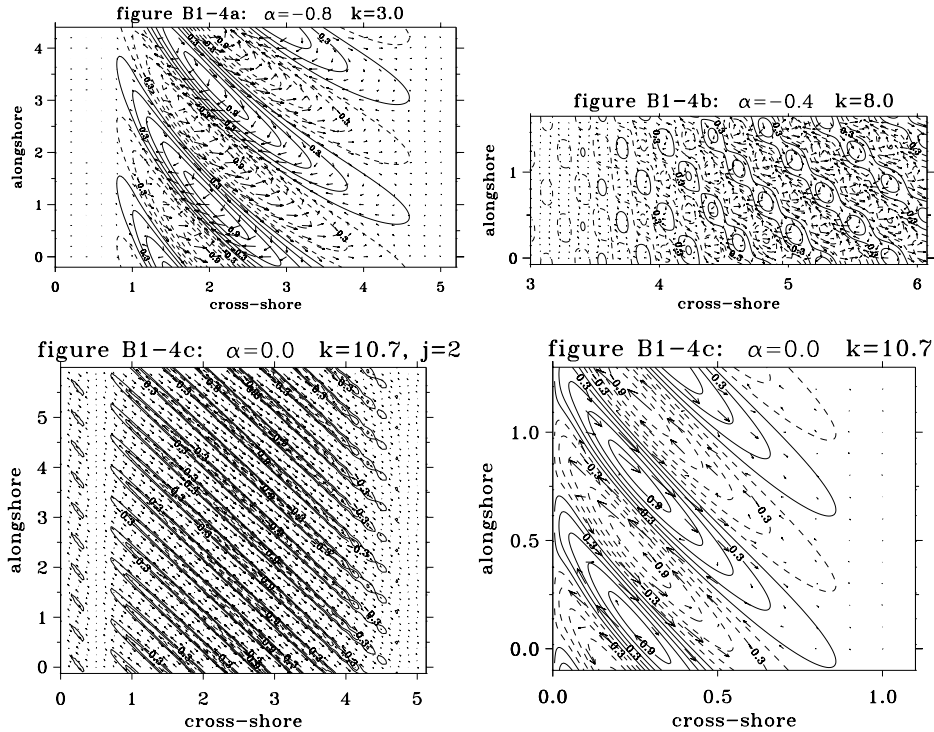

Figure 3.10: Spatial patterns of the most preferred bedforms for different values of parameter α, other parameter values as in figure 3.8. a. $\alpha = -0.8, k = 3.0$. b. $\alpha = -0.4, k = 8.0$. c. $\alpha = 0., k = 10.7$: a trapped tidal sand ridge. d. $\alpha = 0., k = 10.7$: an offshore tidal sandbank.

more the flow profile was chosen such that it exponentially decays in the offshore direction. This was done in order to have no conflict with the boundary conditions in the model which require the perturbations to vanish far offshore. The e-folding lengthscale of the decay was chosen to be

120 km. A motivation for this choice is that on that this is of the order of the external Rossby deformation radius. Using this value, a correct description of the bottom modes was found up to a distance of 50 km from the coast. This exponentially decaying flow structure was also used in chapter 2.

In figure 3.8 a contour plot is shown of the largest growth rate of the perturbations as a function of wavenumber k and parameter α. First of all, a remarkable difference with the storm-dominated case (compare with figure 3.3) is that this plot is nearly symmetric with respect to the line $\alpha = 0$. Hence the direction of the steady current is no longer important for the characteristics of the resulting bedforms. Furthermore, in this plot clearly three different instability regimes can be identified. The first occurs for large values of $|\alpha|$ (nearly steady flow) and is characterized by wavenumbers $k \sim 4$, i.e., longshore spacings of approximately 20 km. A second regime occurs for moderate values of $|\alpha|$ (of order 0.5) and has wavenumbers $k \sim 8$. The final instability regime is observed for small values of $|\alpha|$ (dominant tidal flow) and has wavenumbers $k \sim 10$. In figure 3.9 the wavenumber of the most preferred mode, the maximum growth rate and the migration speed of the most preferred mode are shown as a function of parameter α. Finally, in figure 3.10 contour plots of the most preferred bedforms, together with the perturbed tidally averaged velocity field, are shown for several characteristic preferred modes.

Note that the typical dimensional growth rates are much larger than those in the previous section. However, it should be realized that also the morphologic timescale is now much longer. Hence a dimensionless growth rate of 1 now corresponds to a dimensional e-folding timescale of 6000 yr. Since the nondimensional migration speeds are still of order 1, this implies that the bedforms migrate much slower than in the storm-dominated case: about 2 m yr^{-1}.

The contour plots in figure 3.10 clearly reveal the character of the different preferred modes. For $|\alpha|$ close to 1 the most preferred mode is trapped to the coast and its crests are rotated cyclonically with respect to the dominant current direction. Its formation is related to vorticity production due to Coriolis torques which are exerted if a steady flow is moving over this bar, see chapter 2. The second mode, which can be seen in figure 3.10b, appears on the outer shelf and is characterized by a series of alternating bars and pools. This type of bedform is related to vorticity production induced by frictional torques and it is also observed in case of pure steady flow (see chapter 2).

The third instability regime is linked to the presence of tidal currents and the corresponding bedforms resemble tidal sand ridges, as can be seen in figure 3.10 c,d. Remarkably enough there are two different modes with almost identical growth rates. One corresponds to the classical offshore tidal sandbank which was already described by Huthnance (1982) and Hulscher *et al.* (1993): it occurs on the outer shelf, the crests are rotated cyclonically with respect to the tidal current direction and anticyclonic residual circulations exist around the bars. The other mode appears to be a tidal sand ridge which is trapped to the inner shelf and also has cyclonically rotated crests. However its residual circulation is characterized by strong offshore deflection over the bars, which suggests that its formation is related to the transverse slope mechanism. Indeed experiments (not shown) indicate that the latter mode disappears if the slope s of the inner shelf is reduced.

Another remarkable difference with the storm-dominated case is that the results are not strongly dependent on the value of the parameter a in the steady current profile. If the value of a is reduced (i.e., increasing influence of longshore windstress with respect to longshore pressure gradient) growth rates weakly decrease, but they are still substantially large, even in case $a = 1$. Thus the results discussed here are rather representative for the model; also the sensitivity with respect to the parameter λ^{-1} is rather weak. Furthermore, the sizes of the different instability regions in plots like figure 3.10 depend on the choices for the friction and Coriolis parameter. However, no new phenomena are detected if the values of these coefficients are varied.

3.4.4 Probabilistic mode: experiments with varying β

In this subsection the model is used as a tool to obtain information about the dynamics of bedforms in a probabilistic sense. Thus a shelf is considered on which stormy conditions occur during a time fraction β, whereas in the remaining periods (time fraction $1 - \beta$) the weather is calm. The sediment transport which occurs during these two situations is a linear and a cubic function of the instantaneous velocity, respectively. Besides, the hydrodynamic conditions may also differ during storms and calm weather. This depends on the main direction of waves during storms. If waves approach the coast in a shore-normal direction, physical quantities like the velocity scale U
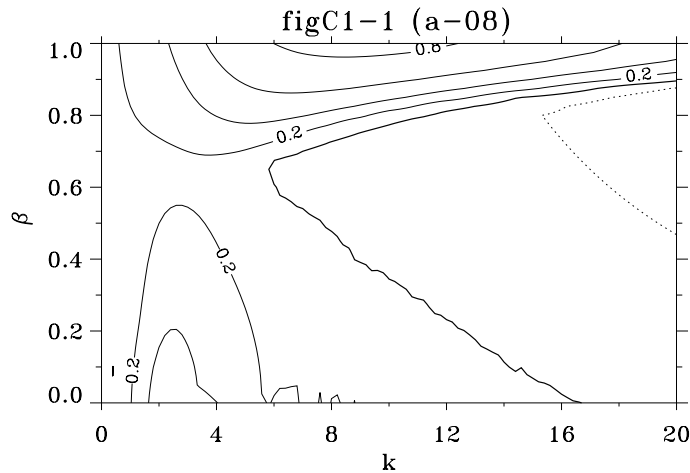
figC1−1 (a−08)

Figure 3.11: Contour plot of the maximum growth rate of perturbations as a function of wavenumber k and the storm fraction parameter β. Here parameter $\alpha = -0.8$, for other values see the text.
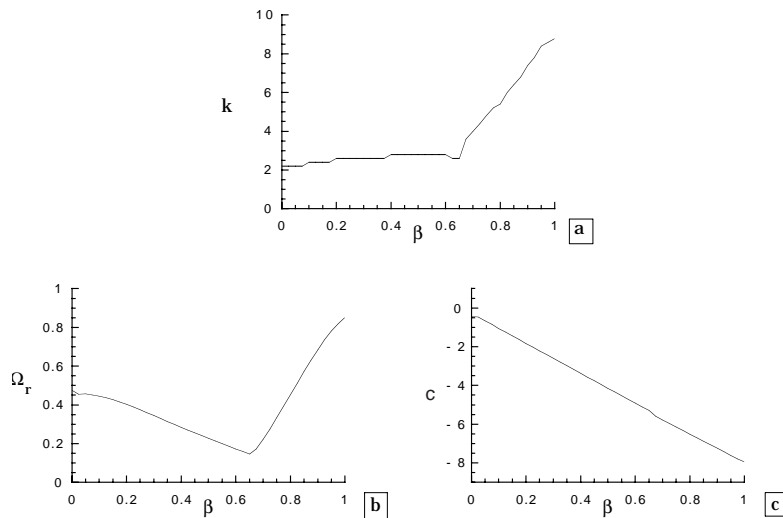

Figure 3.12: a. Wavenumber for which the maximum growth rate is attained as a function of parameter β; other parameter values as in figure 3.11. b. As a., but for the maximum growth rates. c. As a., but the migration speed of the most preferred bedforms.

and the relative contribution of steady and tidal components to the reference flow (indicated by parameter α) will hardly vary. On the other hand, if the wind and waves during storms are mainly directed alongshore, the steady flow (and hence U and α) will be different during different weather conditions.

To understand the behaviour of the probabilistic model the two cases mentioned above will be discussed separately. First the case of 'shore-normal' storms is considered to study the sensitivity of the results to variations in parameter β for different values of α. Once again a shelf with the dimensions and location as discussed in section 3.4.2 is assumed. For stormy conditions the following parameter values were selected: $a = 1, r = 0.2, \hat{\gamma} = 10^{-4}, \lambda^{-1} = 3.4$, whereas during calm weather $a = 0, r = 0.4, \hat{\gamma} = 10^{-3}, \lambda^{-1} = 3.4$. Note that the flow amplitude U during both situations is 0.5 ms^{-1}. The choice of $a = 1$ (i.e., V/H is constant) during storms is quite important, as already found in section 3.4.2, but the choice $a = 0$ for calm weather flow is less important (see section 3.4.3). Finally the ratio of the coefficients ν_1 and ν_3, which indicate the magnitude of the sediment transport during storms and calm weather, had to be selected. From the arguments of section 3.1 and appendix D it follows that $(\nu_1/\nu_3) \gg 1$. In all the experiments discussed below we
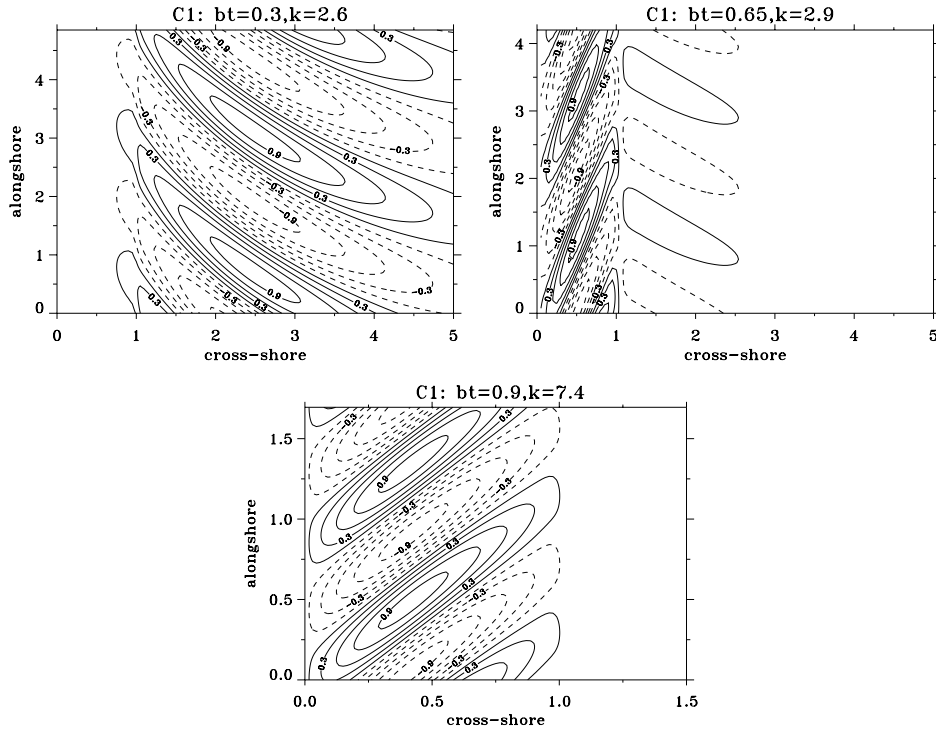
Figure 3.13: Spatial patterns of the most preferred bedforms for different values of parameter β, other parameter values as in figure 3.11. a. $\beta = 0.3, k = 2.6$. b. $\beta = 0.65, k = 2.9$. c. $\beta = 0.9, k = 7.4$.
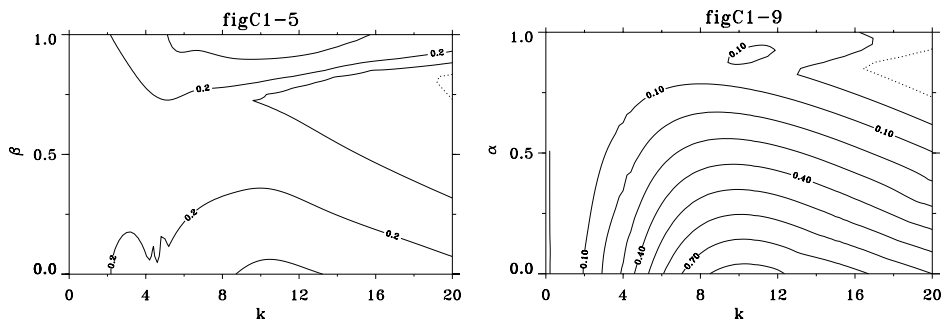

Figure 3.14: Contour plot of the maximum growth rate of perturbations as a function of wavenumber k and the storm fraction parameter β. Here parameter $\alpha = -0.5$ (left) and $\alpha = -0.2$ (right), for other values see the text.

have chosen $(\nu_1/\nu_3) = 10$, which means that the wave-orbital velocity amplitude near the bottom during storms is about three times larger than velocity scale U. Hence in the present case this near-bottom wave velocity amplitude is approximately 0.8 ms^{-1}.

In figure 3.11 a contour plot is shown of the largest growth rate as a function of wavenumber k and storm fraction β for $\alpha = -0.8$. The latter choice implies that the reference flow is directed in the negative y-direction and has a strong steady component. In figure 3.12 the wavenumber, growth rate and migration speed of the most preferred perturbations are shown as a function of β. Clearly, two different instability regimes can be observed in figure 3.11. One occurs for small values of β (dominant calm weather conditions) and has a preferred wavenumber of $k \sim 4$ (corresponding longshore spacings of about 20 km). The second regime is found for large values of β (storms dominate) and the preferred wavenumber $k \sim 9$ (longshore wave-lengths of about 8 km).

As indicated by the figure 3.12 the transition between the two regimes occurs for $\beta \sim 0.7$.
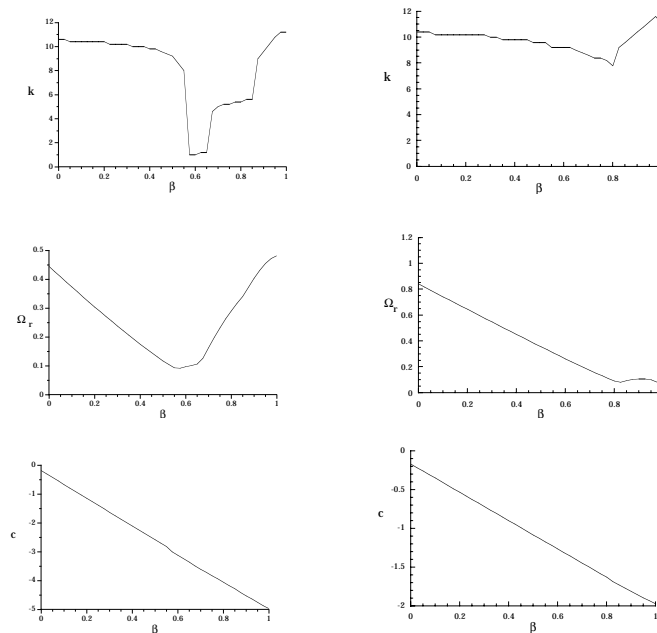
Figure 3.15: **Left**: Wavenumber for which the maximum growth rate (top), the maximum growth rates (bottom left) and the migration speed of the most preferred bedforms (bottom right) is attained as a function of parameter β; $\alpha = -0.5$; other parameter values as in figure 3.14. **Right**: As in the left but for $\alpha = -0.2$.

Contourplots of a few typical preferred modes are shown in figure 3.13. As expected from the analysis of the previous two subsections, for small β (see subplot a) the bottom mode is a Coriolis-induced bar which extends over the inner and outer shelf and has cyclonically rotated crestlines. On the other hand, for large β an upcurrent rotated, trapped shoreface-connected ridge is obtained which, on the Northern Hemisphere, has a different orientation than that of the Coriolis-induced bars and also migrates faster.

It is interesting to observe that if $\beta \sim 0.7$ is selected (figure 3.13c) a preferred mode is predicted which has the characteristics of both shoreface-connected ridges and Coriolis bars. On the outer shelf the bars are cyclonially rotated, whereas on the inner shelf the crest-lines are upcurrent rotated. This is a situation which is also observed on the shelf along the Central Dutch coast, see figure 1.1.

In the next series of experiments the relative contribution of the tidal currents in the reference flow was increased. Results are presented for two different cases: $\alpha = -0.5$ and $\alpha = -0.2$. In figure 3.14 contour plots of the corresponding maximum growth rate in the k, β-parameter space are shown. The dependence of the wavenumber, growth rate and migration speed of the most preferred mode on parameter β is shown in figure 3.15 and the spatial pattern of a few typical bedforms are shown in figure 3.16. From this it follows that always two distinct instability regimes appear which are characterized by small and large β-values, respectively. The transition occurs for $\beta = \beta_c \sim 0.7$, and this value is determined by the choice of the ratio ν_1/ν_3. The characteristics of the preferred bedforms in these regimes depend on the value of α, i.e., on the relative contributions of steady and tidal flow. For $\alpha = -0.5$ (moderate tidal flow) a transition from frictionally-induced alternate bars to shoreface-connected ridges is found, whereas for $\alpha = -0.2$ (strong tidal flow) a transition from offshore tidal sandbanks to trapped tidal ridges is found. For $\beta \sim \beta_c$ the bedforms have characteristics of both these modes.

Subsequently experiments were carried out in which different hydrodynamic conditions during storms and calm weather were modelled. First it was tested whether the model could predict the occurrence of bottom patterns with the characteristics of both shoreface-connected ridges and offshore tidal sandbanks. The parameter values were the same as before, except that for stormy conditions $\alpha = -1$ was chosen and for fair weather conditions $\alpha = 0$. It appeared that, with varying values of the storm fraction β, a transition was found from trapped tidal ridges (near
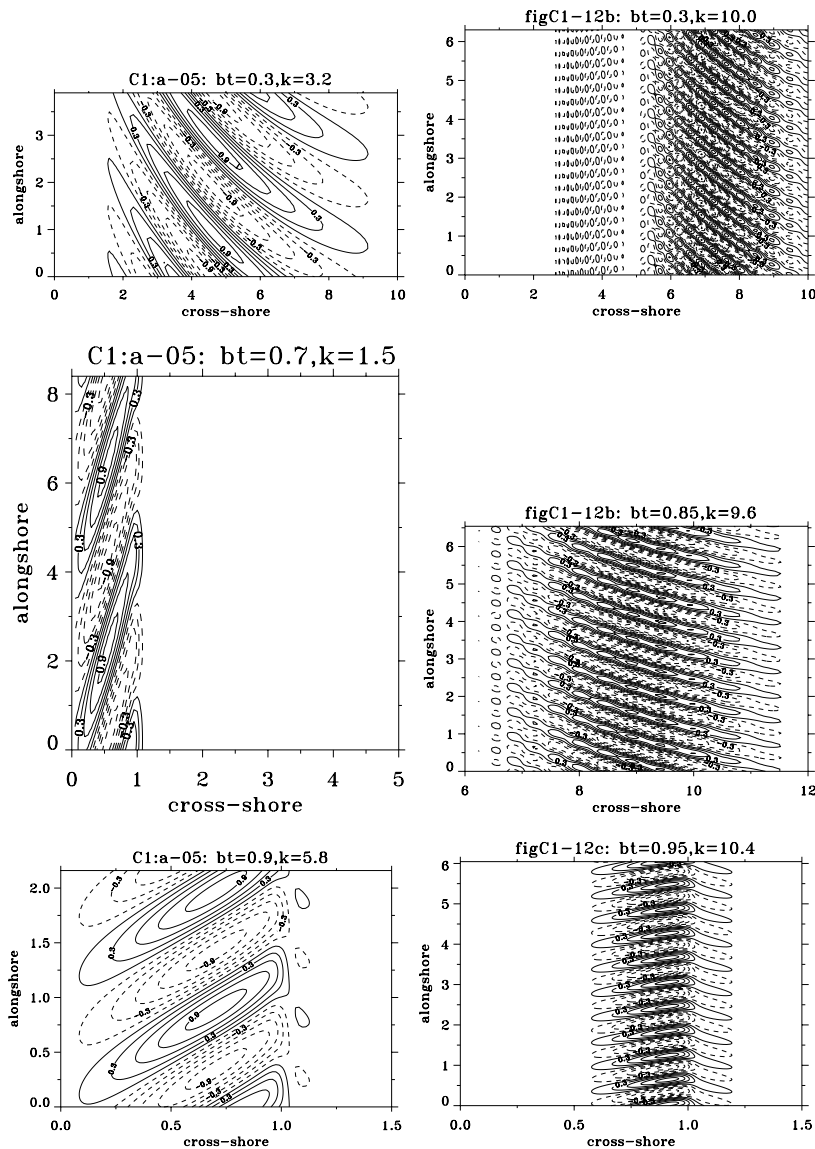
Figure 3.16: Spatial patterns of the most preferred bedforms for different values of parameter β, other parameter values as in figure 3.11. a. $\alpha = -0.5, \beta = 0.3, k = 3.2$. b. $\alpha = -0.2, \beta = 0.3, k = 10.0$. c. $\alpha = -0.5, \beta = 0.7, k = 1.5$. d. $\alpha = -0.2, \beta = 0.85, k = 9.6$. e. $\alpha = -0.5, \beta = 0.9, k = 5.8$. f. $\alpha = -0.2, \beta = 0.95, k = 10.4$.

$\beta = 0$) to shoreface-connected ridges (near $\beta = 1$). However the bedforms for $\beta \sim 0.7$ (not shown) have either the mixed characteristics of a trapped tidal ridge and shoreface-connected ridge or that of pure offshore tidal sandbanks (without morphologic activity on the inner shelf). This suggest that, according to this model, the observed presence of both offshore tidal sandbanks and shoreface-connected ridges cannot be attributed to one preferred mode, which is forming during different weather conditions, but is rather due to the presence of *different* bottom modes which simultaneously develop and have almost equal growth rates.

Finally we carried out experiments in which *both* the velocity scale U and parameter α have different values during different weather conditions. Parameters were chosen to be more or less indicative for the shelf along the central Dutch coast. Here a characteristic depth-averaged tidal current amplitude is $U_t = 0.4$ ms^{-1} and steady current amplitudes during storms and calm weather are of order 0.4 ms^{-1} and 0.1 ms^{-1}, respectively. This yields for storms: $\alpha = -0.5, \lambda^{-1} = 2.215$ and during calm weather $\alpha = -0.2, \lambda^{-1} = 3.4$. Figure 3.17 shows the contour plot of the largest growth rates as a function of k and β. The dependence of wavenumber, growth rate and migration
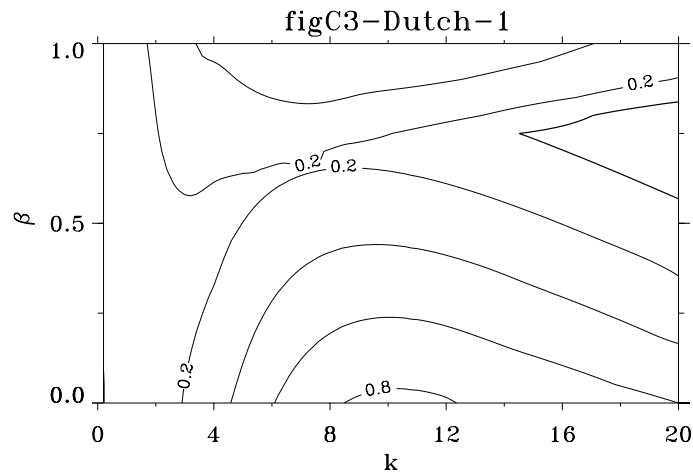
Figure 3.17: Contour plot of the maximum growth rate of perturbations as a function of wavenumber k and the storm fraction parameter β. Here parameters are indicative for the shelf along the central Dutch coast, see the text.
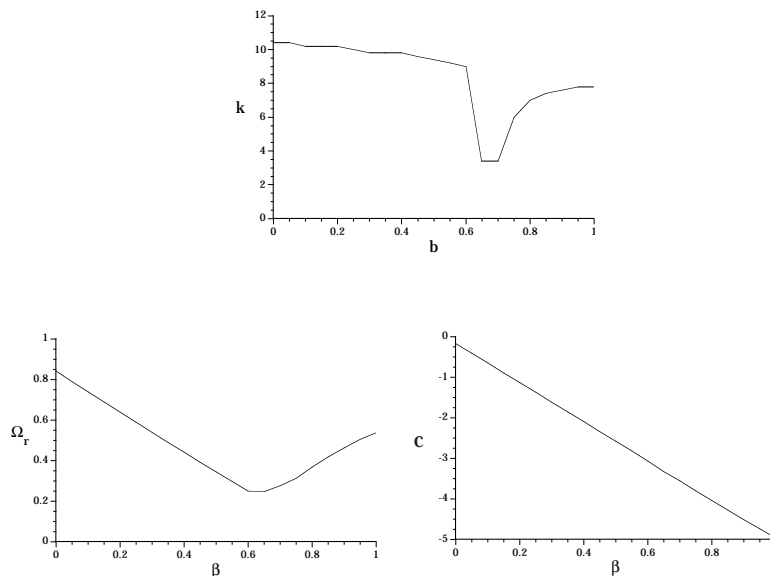

Figure 3.18: Wavenumber for which the maximum growth rate (top), the maximum growth rates (bottom left) and the migration speed of the most preferred bedforms (bottom right) is attained as a function of parameter β; other parameter values as in figure refa2:fig:C3-1.

speed of the most preferred mode are shown in figure 3.18 and contour plots of typical preferred bottom modes are shown in figure 3.19. As can be seen the results are qualitatively similar to the case that $\alpha = -0.5$ both during storms and fair weather, as was discussed above: a transition occurs from frictionally induced alternate bars on the outer shelf to shoreface-connected ridges trapped on the inner shelf. For $\beta \sim 0.6$ two modes exist with almost identical growth rates but different spatial characteristics.

3.5   Physical instability mechanisms

The physical mechanisms underlying the formation of bedforms in the present model can be understood from the analysis of the bottom evolution equation (3.16). As already explained at the end of section 3.4 it basically describes two different instability mechanisms: one related to the trans-
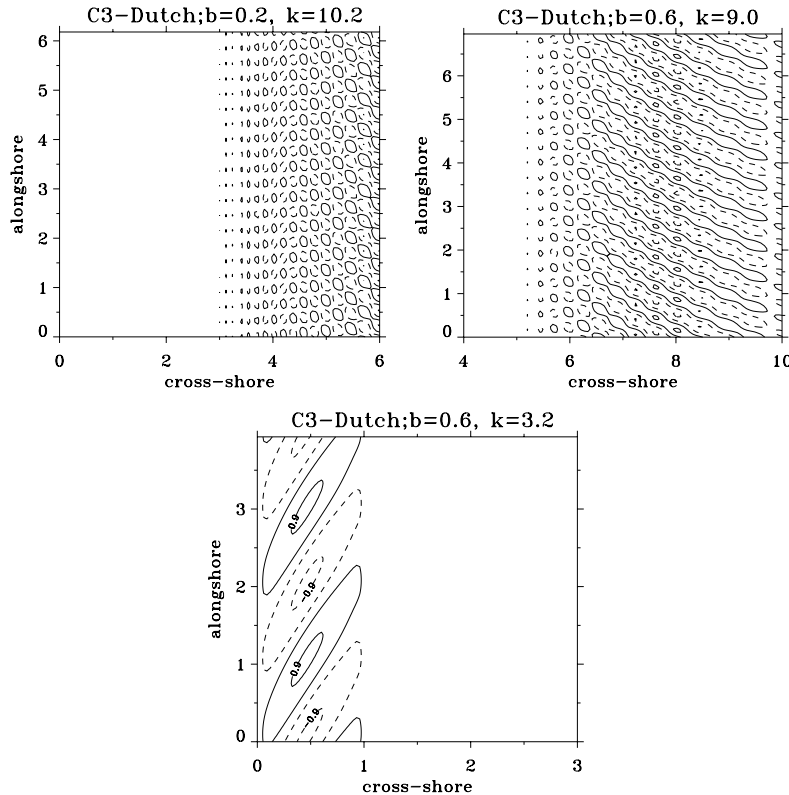
Figure 3.19: Spatial patterns of the most preferred bedforms for different values of parameter β, other parameter values as in figure 3.11. a. $\beta = 0.2, k = 10.2$. b. $\beta = 0.6, k = 3.2$. c. $\beta = 0.6, k = 9.0$.

verse slope of the inner shelf and one related to a 'faster than linear' dependence of the sediment transport on the flow velocity.

The results of the previous section indicate that there are bascially five different types of bedforms generated by the interaction of a combined steady and tidal current and the sandy bottom on the inner and outer shelf. These are shoreface-connected ridges, Coriolis-induced ridges, frictionally-induced alternate bars, offshore tidal sandbanks and tidal ridges which are trapped to the inner shelf. We will now discuss their formation mechanisms.

Shoreface-connected ridges are found for high storm fractions (parameter β close to 1), such that the sediment transport is almost linear, and also for strong steady currents (parameter $|\alpha|$ near 1). These bedforms, which are trapped to the inner shelf, have longshore wavelengths of 5-8 km, they are upcurrent rotated and the flow shows an offshore deflection over the crests. As already discussed by Trowbridge (1995) and in chapter 2 their formation is due to the transverse slope instability mechanism and their length-scale is determined by the width L_s of the inner shelf.

Likewise, the generation of Coriolis- and frictionally induced bars has been explained in chapter 2 by showing that $(\partial u/\partial x)$ becomes positive over a bar due to the production of vorticity by Coriolis and frictional torques if a steady flow moves over these bars. The relevant horizontal lengthscales are $U_s/f \sim 4.5$ km and $U L_v/\mu \sim 6$ km, respectively, where μ is the dimensional linear friction coefficient. The numerical values refer to the parameter settings discussed in the previous section.

The two last bedforms, offshore tidal sandbanks and trapped tidal ridges, are not found in case of a purely steady flow. The former exists only if a 'faster than linear' sediment transport is selected, i.e. $\beta < 1$, see e.g. figure 3.10c. The latter exists for all values of the storm fraction β, as can be seen from the contour plots in figure 3.6d and 3.10d. Their crests are rotated cyclonically with respect to the dominant current direction. Furthermore, their length scales are of the order of the tidal excursion length $(U_t T)/\pi$, which is the distance travelled by a water parcel during a
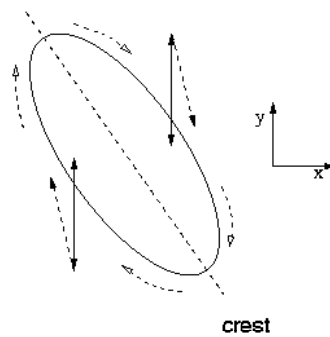
Figure 3.20: Situation sketch (topview) of a tidal flow (solid arrows) over a cylonically rotated ridge on the Northern Hemisphere; reference bottom is flat. Due to tide-topography interaction, see Zimmerman (1981), an anticylonic residual circulation (indicated by dashed arrows) exists around the bank. This causes the upslope flow velocity to be slightly larger than the downslope component. In case of a sediment flux which depends 'faster than linear' on the flow velocity, this results in a net convergence of sediment above the crest.
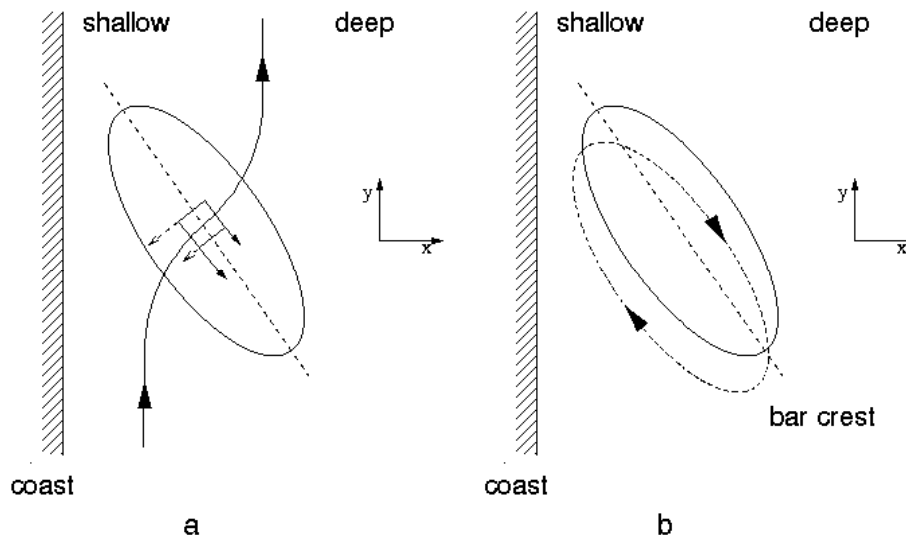

Figure 3.21: a. Situation sketch (topview) of a water parcel moving over a cyclonically rotated bar on a shelf with a transverse slope. The flow bends toward the crest due to continuity effects. At the crest the upper part of the parcel is in deeper water than its lower part. Thus the Coriolis force experienced by the parcel is slightly smaller on the upper part than at the lower part and directed to the right; hence a positive torque occurs (indicated by the solid arrows). Likewise, since the left part of the parcel is in shallower water than the right part, the frictional force on the left side is slightly larger than on the right (indicated by the dahshed arrows). Consequently, also the friction force induces a positive torque. Since velocity component v is positive in this case, the vorticity flux is positive at the crest. b. The net vorticity flux induced by the transverse slope causes a shift in the negative y-direction of the anticyclonic residual circulation (indicated by the dashed contours). Consequently, $u > 0$ above the crest, and instability occurs. For further details see the text.

flood (or ebb) period.

The mechanism causing the generation of offshore tidal sandbanks is rather well-known, but we recapitulate the arguments since they will be used to understand the physics of trapped tidal ridges. As shown by Zimmerman (1981) a tidal flow moving over a cyclonically rotated ridge

generates positive (negative) vorticity, due to both Coriolis and frictional torques, on the down-stream (upstream) part of the ridge. This leads to a net, tidally averaged, convergence of negative vorticity above the crests, as illustrated in figure 3.20. Hence an anticylonic residual circulation (clockwise on the Northern Hemisphere) exists around the ridges. This causes the total velocity of particles moving upslope (downslope) to become slightly larger (smaller). Hence, if the sediment transport is a 'faster than linear' function of the instantaneous flow velocity, the flux will depend on the absolute value of the velocity vector, thereby causing a net convergence of sediment above the crest. In other words, there is a positive feedback between the water motion and the bottom such that the amplitude of the ridge will grow. This mechanism is less effective for anticyclonically rotated ridges, because in that case the Coriolis and frictional torques have opposite signs, such that the residual circulations are much weaker.

The formation of trapped tidal ridges is also closely related to the occurrence of tidal residual circulations, but in this case the instability process is controlled by the transverse slope of the inner shelf. Thus we will analyze the interaction of a tidal flow with a ridge on a tranversely sloping shelf. Again vorticity production due to Coriolis and bottom frictional torques will occur, like in the case of offshore tidal sandbanks. However, as can be seen from the vorticity equation (3.13) and continuity equation (3.14) the transverse slope affects both the planetary vortex stretching (i.e., the Coriolis torque) and the frictional torque. First we consider a cyclonically rotated ridge. If it was located on a flat bed both torques would vanish at the crest and the resulting residual circulation would be anticyclonic around the crests and exactly follow the topographic contours. However, if the undisturbed water depth increases in the offshore direction both the Coriolis torque and frictional torque are such that the net vorticity flux above the crest is positive, see figure 3.21a. Together with the vorticity flux generated due to the sole effect of the ridge (i.e., as if it were located on a flat bottom) it follows that the net vorticity flux due to the transverse slope causes the centre of the anticyclonic residual circulation to shift in the negative y-direction, as indicated in figure 3.21b. Consequently, a positive correlation between the offshore flow component u and the perturbed bottom h occurs and thus the transverse slope mechanism causes a net convergence of sediment above the crests, similar as in the case of shoreface-connected ridges. This shift in the residual circulation and the corresponding positive correlation between u and h is clearly visible in figure 3.6d and 3.10d. Hence the formation of this type of ridges can occur *both* during stormy and fair weather conditions.

Like in case of a flat bed, the transverse slope mechanism is less effective for trapped tidal ridges which are rotated anticyclonically. A similar analysis yields that the Coriolis torque and frictional torque related to the transverse slope cause net vorticity fluxes of opposite sign. Depending on the values of the Coriolis and friction parameters this will result in a weaker offshore (or even onshore) flow component at the bar crests and thus the instability process is weaker.

The previous arguments can also be used to understand the observed asymmetry in figure 3.3 with respect to the line $\alpha = 0$. This indicate that the instability mechanism is more effective for positive values of α (which corresponds to upwelling flow conditions, see section 3.4.2) rather than for negative α-values. This is a consequence of earth rotation which affects both the steady and tidal components of the reference flow. Regarding a steady upwelling flow, its acceleration over a ridge induces an additional offshore-directed Coriolis force. This enhances the offshore deflection of the flow over the bars and thus the transverse slope mechanism becomes more effective. On the contrary, a down-welling flow (in the present model: negative values of α) induces an additional onshore-directed Coriolis force over the bars, such that the transverse slope mechanism is reduced. Also tidal effects are relevant in this respect because it appears from the results of section 3.4.2 that steady upwelling flow induces ridges which are always rotated cyclonically with respect to the dominant currents. This orientation also leads to a strong positive feedback between the bottom and the tidal flow, since in the vorticity equation the torques induced by bottom friction and by the Coriolis force reinforce each other. On the other hand, if the steady flow represents downwelling conditions, both sources of tidal vorticity oppose each other. So in this case, growth rates are smaller, and become even negative for a small downwelling steady current component. Note that the situation for flow along an eastern coast follows by rotating the domain over 180° and the situation on the Southern Hemisphere is obtained by reflection in the x-axis (in the simulations by changing the sign of α).

We also see in figure 3.5a that the preferred wavenumber for positive α are of order 1, so that the dimensional wavelengths are of the order of the tidal excursion $U_t T$, i.e., 20 km. For negative

	weak tides	strong tides
storm dominance	shoreface–connected ridges	trapped tidal ridges
fair weather dominance	Coriolis bars alternate bars	trapped tidal ridges tidal sand banks

Table 3.1: Classification of the five different types of preferred bottom modes predicted by the model. Weak and strong tides refer to values of the α-parameter close to 0 and 1, respectively. Fair weather dominance and storm dominance refer to values of the β-parameter close to 0 and 1, respectively.

α wavenumbers are larger and thus spacings between successive crests are smaller (about 8 km); they are determined by the width of the inner shelf.

3.6   Conclusions

In this chapter an idealized morphodynamic model has been analyzed to study the joint interaction of a steady and tidal flow with the erodible bed on the inner and outer shelf. The first objective was to find out which types of large-scale alongshore rhythmic bottom patterns can form as inherent free instabilities of a coupled water-bottom system. Further aims were to understand the underlying physics of these bedforms and to relate their characteristics to those of morphological features observed in the field.

The water motion in the model is described by the depth-averaged shallow water equations and for the sediment transport a local parametrization is used. A probabilistic concept is used in the sense that the model distinguishes between stormy and calm weather conditions, during which the sediment transport is linear and cubic in the instantaneous velocity, respectively. Apart from that also the effect of local bedslopes on the sediment transport was accounted for.

It appears that the model allows for basically five different types of bedforms: shoreface-connected ridges, Coriolis-induced ridges, frictionally-induced bars, offshore tidal sandbanks and trapped tidal ridges. They occur for different values of the tidal parameter α and the storm fraction parameter β, as is summarized in table 3.1 .

The formation of shoreface-connected ridges, which are trapped to the inner shelf and have up-current rotated crest-lines, occurs most effectively during stormy conditions and with a strong steady flow component, see also Trowbridge (1995) and chapter 2. Predicted spatial patterns and timescale are in satisfactory agreement with field data. Their formation is related to the presence of the transverse slope of inner shelf and is strongly influenced by tidal effects. If for a fixed steady current the amplitude of the tidal current is increased the growth rates become larger, longshore spacings become longer and the orientation of the crest-lines changes from upcurrent to cyclonic. For strong tidal currents the preferred bedform becomes a trapped tidal sand ridge, a feature which has not been described in earlier studies. It owes its existence to the shift of tidal residual circulations due to the transverse slope of the inner shelf, as explained in section 3.5 of this chapter.

Coriolis-induced ridges mainly form during calm weather and dominant steady current; with increasing tidal influence (or increasing the value of the bottom friction coefficient) frictionally-induced alternate bars are predicted. These two modes are modifications of bedforms which were already identified and explained in chapter 2. For strong tidal currents and a 'faster than linear' sediment transport offshore tidal sandbanks occur, which were modelled by Huthnance (1982) and Hulscher $et~al.$ (1993).

The ultimate structure of the bedforms strongly depends on the value of the storm fraction parameter β. For β smaller than a critical value β_c the preferred bedforms primarily form during calm weather conditions. In our simulations the value of β_c is about 0.6-0.8; this depends on the choice of the morphological timescales during calm weather and storms, respectively. For β somewhat larger than β_c the preferred bedforms have more the characteristics of storm-dominated features. In the transition regime $\beta \sim \beta_c$ the spatial pattern of the bottom modes has characteristics of both types of bedforms. This suggests that the simultaneous presence of offshore tidal sandbanks and shoreface-connected ridges on the shelf along the central Dutch coast can be understood from

the characteristics of one preferred mode, which is forming during different weather conditions. However, a series of model experiments has shown that such type of behaviour is only observed for strong steady currents. In case that tidal effects dominate the simultaneous presence of different bottom modes can only be explained as the result of the growth of *different* bottom modes which have almost identical growth rates.

It is remarkable that the model predicts five different types of preferred bottom modes, whereas only two of them (shoreface-connected ridges and offshore tidal sandbanks) are well-known from field observations. This is probably due to the fact that the parameter values for which the other bedforms are most favourably excited correspond to situations which usually do not occur in nature. Indeed most shelves are either storm-dominated and characterized by strong steady currents (like the US and Argentinian shelf) or calm weather conditions prevail together with strong tidal currents (like the outer shelf of the North Sea).

The model is also subject to a number of limitations which deserve further attention. First of all, it seems that quite small values of the bedslope coefficient $\hat{\gamma}$ has to be assumed during stormy conditions in order to obtain realistic spacings of shoreface-connected ridges. This appears to be due to the formulation of the bedslope correction term in the sediment transport. As shown in a recent study by Walgreen (1999) it appears the effective diffusion coefficient during storm is not $\hat{\gamma}|V|$, as in the present model, but rather a constant effective diffusion coefficient, which has a value of about 3 times larger than the present value of γ. The reason that we have not adopted this formulation in the present study is to keep an as close as possible connection with the study of chapter 2 in which also a diffusion coefficient proportional to $\hat{\gamma}|V|$ was assumed. Moreover, the qualitative results of the model do not depend on this particular choice.

Another limitation is that the model is based on spatially uniform wave conditions during storms. In other words, parameters like the 'wave stirring coefficient' ν_1, bedslope coefficient γ and bottom friction parameter during storms are assumed to be constant. In reality these will be functions of the water depth and this may have quite a substantial effect on the dynamics of the bedforms. However, results of Walgreen (1999) indicate that, for suitable and realistic choices of the depth dependencies, the main conclusions are found in the present chapter are recovered.

The reference flow in the present model consists of a steady component and one tidal constituent; overtides are only generated internally due to tide-topography interaction. However, both observations and models of tidal currents in the North Sea, cf. Sinha & Pingree (1997), demonstrate that the water motion along the central part of the Dutch coast also has a strong external M_4-component. Thus it is worthwhile to investigate the sensitivity of model results to incorporation of this second tidal harmonic. It should be realized that the discussion in appendix E indicates that this is quite a substantial amount of work.

Finally note that the present study is limited to a linear analysis. In other words, the model only describes the initial formation of the bedforms and it yields no information about the amplitude behaviour of the ridges. In order to describe the long-term behaviour of bedforms the model has to be extended into the nonlinear regime. This will be done in chapter 4, based on a method in which the solution is expanded in eigenfunctions of the linear stability analysis. The analysis is restricted to shoreface-connected ridges on a storm-dominated shelf with steady currents only. Hence it seems that the present model set-up and results contribute to a further understanding of the dynamics of sand ridges on the inner and outer shelf.